Optical Coherence Elastography Needle for Biomechanical Characterization of Deep Tissue

Robin Mieling(✉) , Sarah Latus, Martin Fischer, Finn Behrendt
and Alexander Schlaefer

Institute of Medical Technology and Intelligent Systems,
Hamburg University of Technology, Hamburg, Germany
`robin.mieling@tuhh.com`

Abstract. Compression-based optical coherence elastography (OCE) enables characterization of soft tissue by estimating elastic properties. However, previous probe designs have been limited to surface applications. We propose a bevel tip OCE needle probe for percutaneous insertions, where biomechanical characterization of deep tissue could enable precise needle placement, e.g., in prostate biopsy. We consider a dual-fiber OCE needle probe that provides estimates of local strain and load at the tip. Using a novel setup, we simulate deep tissue indentations where frictional forces and bulk sample displacement can affect biomechanical characterization. Performing surface and deep tissue indentation experiments, we compare our approach with external force and needle position measurements at the needle shaft. We consider two tissue mimicking materials simulating healthy and cancerous tissue and demonstrate that our probe can be inserted into deep tissue layers. Compared to surface indentations, external force-position measurements are strongly affected by frictional forces and bulk displacement and show a relative error of 49.2% and 42.4% for soft and stiff phantoms, respectively. In contrast, quantitative OCE measurements show a reduced relative error of 26.4% and 4.9% for deep indentations of soft and stiff phantoms, respectively. Finally, we demonstrate that the OCE measurements can be used to effectively discriminate the tissue mimicking phantoms.

Keywords: Optical Coherence Tomography · Tissue Elasticity · Prostate Biopsy

1 Introduction

Healthy and cancerous soft tissue display different elastic properties, e.g. for breast [19], colorectal [7] and prostate cancer [4]. Different imaging modalities

can be used to detect the biomechanical response to an external load for the characterization of cancerous tissue, e.g., ultrasound, magnetic resonance and optical coherence elastography (OCE). The latter is based on optical coherence tomography (OCT), which provides excellent visualization of microstructures and superior spatial and temporal resolution in comparison to ultrasound or magnetic resonance elastography [8]. One common approach for quantitative OCE is to determine the elastic properties from the deformation of the sample and the magnitude of a quasi-static, compressive load [10]. However, due to the attenuation and scattering of the near-infrared light, imaging depth is generally limited to approximately 1 mm in soft tissue. Therefore, OCE is well suited for sampling surface tissue and commonly involves bench-top imaging systems [26], e.g. in ophthalmology [21,22] or as an alternative to histopathological slice examination [1,16]. Handheld OCE systems for intraoperative assessment [2,23] have also been proposed. While conventional OCE probes have been demonstrated at the surface, regions of interest often lie deep within the soft tissue, e.g., cancerous tissue in percutaneous biopsy.

Taking prostate cancer as an example, biomechanical characterization could guide needle placement for improved cancer detection rates while reducing complications associated with increased core counts, e.g. pain and erectile dysfunction [14,18]. However, the measurement of both the applied load and the local sample compression is challenging. Friction forces superimpose with tip forces as the needle passes through tissue, e.g., the perineum. Furthermore, the prostate is known to display large bulk displacement caused by patient movement and needle insertions [20,24] in addition to actual sample compression (Fig. 1, left). Tip force sensing for estimating elastic properties has been proposed [5] but bulk tissue displacement of deep tissue was not considered. In principle, compression and tip force could be estimated by OCT. Yet, conventional OCE probes typically feature flat tip geometry [13,17].

To perform OCE in deep tissue structures, we propose a novel bevel tip OCE needle design for the biomechanical characterization during needle insertions. We consider a dual-fiber setup with temporal multiplexing for the combined load and compression sensing at the needle tip. We design an experimental setup that can simulate friction forces and bulk displacement occurring during needle biopsy (Fig. 1). We consider tissue-mimicking phantoms for surface and deep tissue indentation experiments and compare our results with force-position curves externally measured at the needle shaft. Finally, we consider how the obtained elasticity estimates can be used for the classification of both materials.

2 Methods

In the following, we first present our OCE needle probe and outline data processing for elasticity estimates. We then present an experimental setup for simulating friction and bulk displacement and describe the conducted surface and deep tissue indentation experiments.

2.1   OCE Needle for Deep Tissue Indentation

Our OCE needle approach is illustrated in Fig. 2. It consists of an OCT imaging system, a time-division multiplexer and our OCE needle probe. The needle features two single-mode glass fibers (SMF-28, Thorlabs GmbH, GER) embedded into a bevel tip needle. The forward viewing fiber (Fiber 1) images sample compression while the load sensing fiber (Fiber 2) visualizes the displacement of a reference epoxy layer that is deformed under load. We cleave the distal ends of both fibers to enable common path interference imaging. The outer diameter of the OCE needle prototype is 2.0 mm. We use a spectral domain OCT imaging system (Telesto I, Thorlabs GmbH, GER) with a center wavelength λ_0 of 1325 nm to acquire axial scans (A-scans) at a sampling rate of 91.3 kHz. A solid state optical switch (NSSW 1x2 NanoSpeed^{TM}, Agiltron, USA), a 100 kHz switch driver (SWDR DC-100KHz NS Driver, Agiltron, USA) and a microcontroller (Arduino^{TM} Mega 2560, Arduino, USA) alternate between the two fibers every second A-scan. Compared to spatial multiplexing [17], our temporal multiplexing maximizes the field-of-view and signal strength while effectively halving the acquisition frequency.
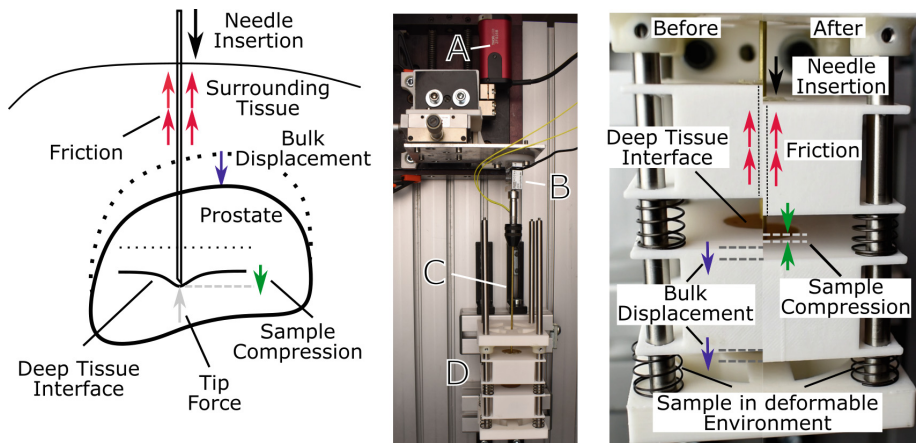

Fig. 1. Left: Schematic of deep tissue indentation during needle insertion. Friction forces (red) and tip forces (grey) are superimposed and the forward motion of the needle (black) only partially results in sample compression (green) due to bulk displacement (blue). Middle: Experimental setup used for indentation experiments, with a linear actuator (A), an axial force sensor (B), the OCE needle probe (C) and the sample layers (D). Right: Simulated deep tissue indentation before and after needle motion. Friction can be added by puncturing multiple layers and bulk displacement is simulated by placing the sample on springs. (Color figure online)

2.2 OCE Measurement

In unconfined compression, the elasticity of the sample can be determined by the relation between stress σ and bulk strain ϵ denoted by the Young's modulus
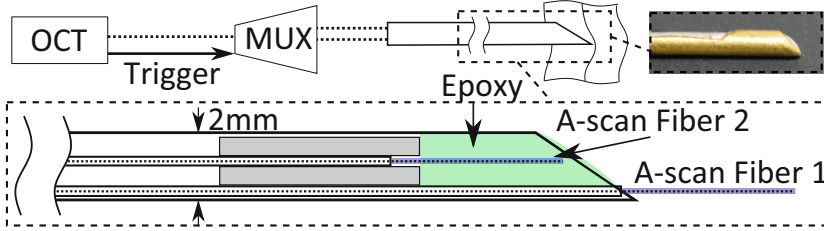

Fig. 2. Illustration of our OCE needle probe for deep tissue indentation. Axial scans (blue) are alternately recorded from fiber 1 and 2 with the OCT and multiplexer (MUX) setup. We use optical fiber 1 to measure sample compression and fiber 2 for the displacement of a reference epoxy layer (green) that is deformed under tip forces. (Color figure online)

$$E = \frac{\sigma}{\epsilon} = \frac{F/A}{\Delta L/L_0}, \tag{1}$$

with the force F, the area A, initial sample length L_0 and assuming incompressibility, quasi-static loading and neglecting viscoelasticity. However, the indentation with our bevel tipped needle will not result in uniform stress and we hypothesize instead that the elasticity is only relative to the applied tip force F_T and the resulting local strain ϵ_l. To obtain a single parameter for comparing two measurements, we assume a linear relation

$$E_{OCE}(F_T, \epsilon_l) \approx \frac{F_T}{\epsilon_l} \tag{2}$$

in the context of this work. To detect strain (Fiber 1) and applied force (Fiber 2), we consider the phase ϕ of the complex OCT signals for fiber i at time t and depth z. The phase shift between two A-scans is proportional to the depth dependent displacement $\delta u_i(z,t)$

$$\delta\phi_i(z,t) = \frac{4\,\pi\,n\,\delta u_i(z,t)}{\lambda_0}, \tag{3}$$

assuming a refractive index n of 1.45 and 1.5 for tissue (Fiber 1) and epoxy (Fiber 2), respectively. We obtain the deformation $u_i(z,t)$ from the unwrapped phase and perform spatial averaging to reduce noise. For fiber 1, we employ a moving average with a window size of 0.1 mm. We estimate local strain based on the finite difference along the spatial dimension over an axial depth Δz of 1 mm.

$$\epsilon_l(t) = \frac{u_1(z_0 + \Delta z, t) - u_1(z_0, t)}{\Delta z} \tag{4}$$

For fiber 2, we calculate the mean $\bar{u}_2(t)$ over the entire depth of the epoxy. We assume a linear coefficient a_F to model the relation between the applied tip force F_T and the mean deformation $\bar{u}_2$ of the reference epoxy layer.

$$F_T(t) = a_F * \bar{u}_2(t). \tag{5}$$

2.3   Experimental Setup

We build an experimental setup for surface and deep tissue indentations with simulated force and bulk displacement (Fig. 1). For deep tissue indentations, different tissue phantoms are stacked on a sample holder with springs in between. For surface measurements, we position the tissue phantoms separately without additional springs or tissue around the needle shaft. We use a motorized linear stage (ZFS25B, Thorlabs GmbH, GER) to drive the needle while simultaneously logging motor positions. An external force sensor (KD24s 20N, ME-Meßsysteme GmbH, GER) measures combined axial forces. We consider two gelatin gels as tissue mimicking materials for healthy and cancerous tissue. The two materials (Mat. A and Mat. B) display a Young's modulus of 53.4 kPa and 112.3 kPa, respectively. Reference elasticity is determined by unconfined compression experiments of three cylindrical samples for each material according to Eq. 1, using force and position sensor data (See supplementary material). The Young's modulus is obtained by linear regression for the combined measurements of each material. We calibrate tip force estimation (Fiber 2) by indentation of silicone samples with higher tear resistance to ensure that no partial rupture has taken place. We
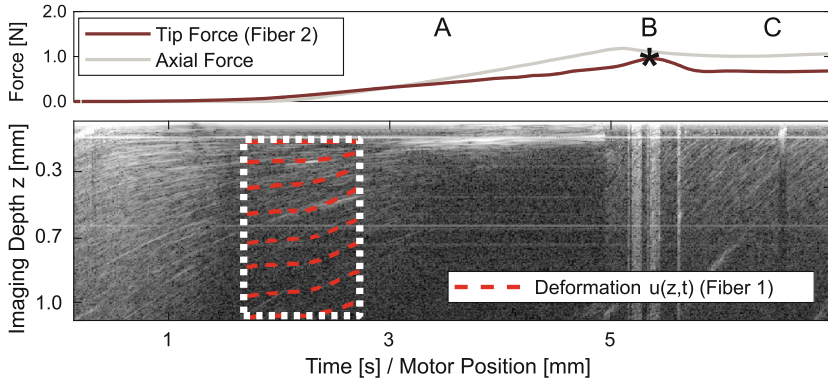

Fig. 3. Demonstration of the dual-fiber needle in insertion with puncture event (B) and post-rupture cutting phase (C). The needle is inserted with a velocity of $1\,\mathrm{mm\,s^{-1}}$. Visualization of the magnitude of the complex OCT signal from fiber 1 (bottom) displayed over needle motion/time. Estimated tip forces from fiber 2 and axial forces are displayed at the top. Acquisition window during pre-deformation phase (A) considered for OCE measurements is indicated by dashed white line. Local strain is calculated based on the tracked deformation from the OCT phase difference as visualized in red.

then determine a linear fit according to Eq. 5 and obtain $a_F = 174.4\,\mathrm{mN\,mm^{-1}}$ from external force sensor and motor position measurements (See supplementary material).

2.4   Indentation Experiments

In total, we conduct ten OCE indentation measurements for each material. Three surface measurements with fixed samples and seven deep tissue indentations with simulated friction and bulk displacement. For each indentation, we place the needle in front of the surface or deep tissue interface and acquire OCT data while driving the needle for 3 mm (Fig. 1). As the beginning of the needle movement might not directly correspond to the beginning of sample indentation, we evaluate OCE measurements only if the estimated tip force is larger than 50 mN. To further ensure that measurements occur within the pre-rupture deformation phase [6,15], only samples below 20 % local strain are considered. A visualization of the OCE acquisition window from an example insertion with surface rupture and post-rupture cutting phase [6,15] is shown in Fig. 3. We evaluate external needle shaft measurements of relative axial force and relative motor position with the same endpoint obtained from local strain estimates. We perform linear regression to determine the slopes $E_{OCE}[\mathrm{mN\,\%^{-1}}]$ and $E_{EXT}[\mathrm{mN\,mm\%^{-1}}]$ from tip-force-strain and axial-force-position curves, respectively. As we can consider surface measurements as equivalents to the known elasticity, we regard the relative error (RE) of the mean value obtained for deep indentations, with respect to the average estimate during surface indentations. We report the RE
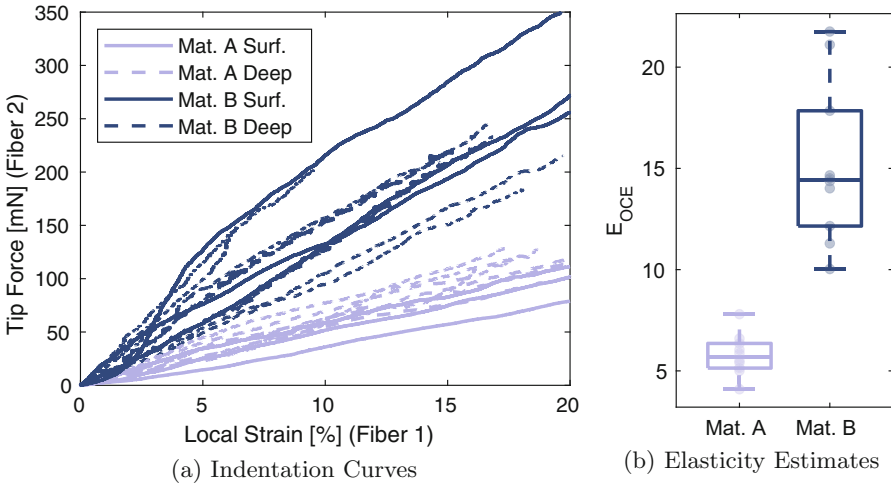

(a) Indentation Curves

(b) Elasticity Estimates

Fig. 4. (a) OCE needle measurements for surface and deep tissue indentations based on the estimated tip force (fiber 2) and the detected local strain (fiber 1). (b) Resulting OCE elasticity estimates show good separation between the two materials, enabling quantitative biomechanical characterization during deep tissue indentations.
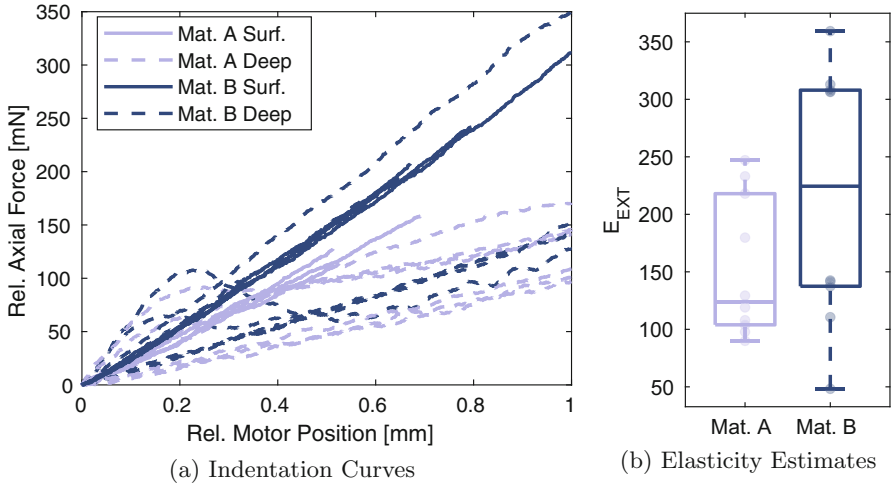
Fig. 5. (a) Axial force-position-curves for surface and deep tissue indentations from external force sensor and motor encoder. Friction increases the measured axial force, while bulk displacement decreases the observed slope. Bulk displacement can occur suddenly due to stick-slip, as seen in two cases of material B. (b) Resulting elasticity estimates show overlap between the two materials, hampering quantitative biomechanical characterization.

for both OCE and external measurements and material A and B, respectively. Finally, we consider the measured elasticities for the biomechanical classification of the material. We report the area under the receiver operating characteristic (AUROC) and area under the precision recall curve (AUPRC) for both external and OCE sensing.

3   Results

The OCE measurements for surface and deep tissue indentations are displayed in Fig. 4a. In comparison, external force-position curves are shown in Fig. 5a. The resulting estimates E_{OCE} and E_{EXT} are shown in Fig. 4b and Fig. 5b, respectively. It can be seen that OCE measurements result in separation of both materials while an overlap is visible for external sensors. The sample elasticities and relative error are also accumulated in Table 1. Biomechanical characterization based on the OCE estimates allows complete separation between materials, with AUROC and AUPRC scores of 1.00 (See supplementary material). External measurements do not enable robust discrimination of materials and yielded AUROC and AUPRC scores of only 0.85 and 0.861, respectively.

4   Discussion and Conclusion

We demonstrate our approach on two tissue mimicking materials that have similar elastic properties as healthy and cancerous prostate tissue [5,11]. The con-

Table 1. Measured elasticity E_{OCE} and external sensors E_{EXT} for both materials with sample size n. We also report the relative error (RE) between the mean values obtained from surface and deep tissue indentations.

		E_{OCE} [mN %$^{-1}$]			E_{EXT} [mN mm^{-1}]			n
		Mean	Min	Max	Mean	Min	Max	
Mat. A	Surf	4.87 ± 0.72	4.04	5.42	232.7 ± 14.6	217.97	247.08	3
	Deep	6.18 ± 0.87	5.05	7.80	118.26 ± 3.01	89.99	179.75	7
	RE	26.4 %			49.2 %			
Mat. B	Surf	14.92 ± 3.28	12.10	18.53	361.02 ± 6.94	353.37	366.92	3
	Deep	15.39 ± 4.48	10.02	21.75	201.31 ± 89.04	136.56	354.60	7
	RE	4.9 %			42.4 %			

ducted indentation experiments demonstrate the feasibility of OCE elasticity estimates for deep tissue needle insertions. OCE estimates show better agreement between surface and deep tissue indentations compared to external measurements, as displayed by reduced relative errors of 26.4% and 4.9% for both phantoms, respectively. Bulk displacement causes considerate underestimation of elasticity estimates when only needle position and axial forces are considered, shown by relative errors of 49.2% and 42.4% for material A and B, respectively. Additionally, quantitative OCE estimates allow the robust discrimination between the two materials as shown by Fig. 4b and the AUROC and AUPRC scores of 1. Note that the high errors for external measurements at the needle shaft are systematic, as friction and bulk displacement are unknown. In contrast, our probe does not suffer from these systematic errors. Moreover, considering the standard deviation for OCE estimates, improved calibration of our dual-fiber needle probe is expected to further improve performance. Deep learning-based approaches for tip force estimation could provide increased accuracy and sensitivity compared to the assumed linear model [3]. Weighted strain estimation based on OCT signal intensity [26] could address the underestimation of local strain during segments of low signal-to-noise-ratio (See supplementary material). We are also currently only considering the loading cycle and linear elastic models for our approach. However, soft-tissue displays strong non-linearity in contrast to the mostly linear behavior of gelatin gels. Compression OCE theoretically enables the analysis of non-linear elastic behavior [26] and future experiments will consider non-linear models and unloading cycles better befitting needle-tissue-interaction [15,25].

Interestingly, our needle works with a beveled tip geometry that allows insertion into deep tissue structures. During insertion, tip force estimation can be used to detect interfaces and select the pre-rupture deformation phase for OCE estimates (Fig. 3). This was previously not possible with flat tip needle probes [9,13,17]. While the cylindrical tip is advantageous for calculating the

Young's modulus, it has been shown that the calculation of an equivalent Young's modulus is rarely comparable across different techniques and samples [4,12]. Instead, it is important to provide high contrast and high reproducibility to reliably distinguish samples with different elastic properties. We show that our dual-fiber OCE needle probe enables biomechanical characterization by deriving quantitative biomechanical parameters as demonstrated on tissue mimicking phantoms. Further experiments need to include biological soft tissue to validate the approach for clinical application, as our evaluation is currently limited to homogeneous gelatin. This needle probe could also be very useful when considering robotic needle insertions, e.g., to implement feedback control based on elasticity estimates.

References

1. Allen, W.M., et al.: Wide-field quantitative micro-elastography of human breast tissue. Biomed. Opt. Express **9**(3), 1082–1096 (2018). https://doi.org/10.1364/BOE.9.001082

2. Fang, Q., et al.: Handheld probe for quantitative micro-elastography. Biomed. Opt. Express **10**(8), 4034–4049 (2019). https://doi.org/10.1364/BOE.10.004034

3. Gessert, N., et al.: Needle tip force estimation using an OCT fiber and a fused convGRU-CNN architecture. In: Frangi, A.F., Schnabel, J.A., Davatzikos, C., Alberola-López, C., Fichtinger, G. (eds.) MICCAI 2018. LNCS, vol. 11073, pp. 222–229. Springer, Cham (2018). https://doi.org/10.1007/978-3-030-00937-3_26

4. Good, D.W., et al.: Elasticity as a biomarker for prostate cancer: a systematic review. BJU Int. **113**(4), 523–534 (2014). https://doi.org/10.1111/bju.12236

5. Iele, A., et al.: Miniaturized optical fiber probe for prostate cancer screening. Biomed. Opt. Express **12**(9), 5691–5703 (2021). https://doi.org/10.1364/BOE.430408

6. Jiang, S., Li, P., Yu, Y., Liu, J., Yang, Z.: Experimental study of needle-tissue interaction forces: effect of needle geometries, insertion methods and tissue characteristics. J. Biomech. **47**(13), 3344–3353 (2014). https://doi.org/10.1016/j.jbiomech.2014.08.007

7. Kawano, S., et al.: Assessment of elasticity of colorectal cancer tissue, clinical utility, pathological and phenotypical relevance. Cancer Sci. **106**(9), 1232–1239 (2015). https://doi.org/10.1111/cas.12720

8. Kennedy, B.F., Kennedy, K.M., Sampson, D.D.: A review of optical coherence elastography: fundamentals, techniques and prospects (2014). https://doi.org/10.1109/JSTQE.2013.2291445

9. Kennedy, K.M., et al.: Needle optical coherence elastography for the measurement of microscale mechanical contrast deep within human breast tissues. J. Biomed. Opt. **18**(12), 121510 (2013). https://doi.org/10.1117/1.JBO.18.12.121510

10. Kennedy, K.M., et al.: Quantitative micro-elastography: imaging of tissue elasticity using compression optical coherence elastography. Sci. Rep. **5**(Apr), 1–12 (2015). https://doi.org/10.1038/srep15538

11. Krouskop, T.A., Wheeler, T.M., Kallel, F., Garra, B.S., Hall, T.: Elastic moduli of breast and prostate tissues under compression. Ultrason. Imaging **20**(4), 260–274 (1998). https://doi.org/10.1177/016173469802000403

12. McKee, C.T., Last, J.A., Russell, P., Murphy, C.J.: Indentation versus tensile measurements of young's modulus for soft biological tissues. Tissue Eng. Part B Rev. **17**(3), 155–164 (2011). https://doi.org/10.1089/ten.TEB.2010.0520

13. Mieling, R., Sprenger, J., Latus, S., Bargsten, L., Schlaefer, A.: A novel optical needle probe for deep learning-based tissue elasticity characterization. Curr. Dir. Biomed. Eng. **7**(1), 21–25 (2021). https://doi.org/10.1515/cdbme-2021-1005

14. Oderda, M., et al.: Accuracy of elastic fusion biopsy in daily practice: results of a multicenter study of 2115 patients. Int. J. Urol. **25**(12), 990–997 (2018). https://doi.org/10.1111/IJU.13796

15. Okamura, A.M., Simone, C., O'Leary, M.D.: Force modeling for needle insertion into soft tissue. IEEE Trans. Biomed. Eng. **51**(10), 1707–1716 (2004). https://doi.org/10.1109/TBME.2004.831542

16. Plekhanov, A.A., et al.: Histological validation of in vivo assessment of cancer tissue inhomogeneity and automated morphological segmentation enabled by optical coherence elastography. Sci. Rep. **10**(1), 11781 (2020). https://doi.org/10.1038/s41598-020-68631-w

17. Qiu, Y., et al.: Quantitative optical coherence elastography based on fiber-optic probe for in situ measurement of tissue mechanical properties. Biomed. Opt. Express **7**(2), 688 (2016). https://doi.org/10.1364/boe.7.000688

18. Rosenkrantz, A.B., et al.: Prostate magnetic resonance imaging and magnetic resonance imaging targeted biopsy in patients with a prior negative biopsy: a consensus statement by AUA and SAR. J. Urol. **196**(6), 1613–1618 (2016). https://doi.org/10.1016/j.juro.2016.06.079

19. Samani, A., Zubovits, J., Plewes, D.: Elastic moduli of normal and pathological human breast tissues: an inversion-technique-based investigation of 169 samples. Phys. Med. Biol. **52**(6), 1565 (2007)

20. Schouten, M.G., et al.: Evaluation of a robotic technique for transrectal MRI-guided prostate biopsies. Eur. Radiol. **22**(2), 476–483 (2012). https://doi.org/10.1007/s00330-011-2259-3

21. Singh, M., Nair, A., Aglyamov, S.R., Larin, K.V.: Compressional optical coherence elastography of the cornea. Photonics **8**(4), 111 (2021). https://doi.org/10.3390/photonics8040111

22. de Stefano, V.S., Ford, M.R., Seven, I., Dupps, W.J.: Live human assessment of depth-dependent corneal displacements with swept-source optical coherence elastography. PLoS ONE **13**(12), e0209480 (2018). https://doi.org/10.1371/journal.pone.0209480

23. Wang, X., Wu, Q., Chen, J., Mo, J.: Development of a handheld compression optical coherence elastography probe with a disposable stress sensor. Opt. Lett. **46**(15), 3669 (2021). https://doi.org/10.1364/ol.429955

24. Xu, H., et al.: MRI-guided robotic prostate biopsy: a clinical accuracy validation. In: Jiang, T., Navab, N., Pluim, J.P.W., Viergever, M.A. (eds.) MICCAI 2010. LNCS, vol. 6363, pp. 383–391. Springer, Heidelberg (2010). https://doi.org/10.1007/978-3-642-15711-0_48

25. Yang, C., Xie, Y., Liu, S., Sun, D.: Force modeling, identification, and feedback control of robot-assisted needle insertion: a survey of the literature. Sensors **18**(2) (2018). https://doi.org/10.3390/S18020561
26. Zaitsev, V.Y., et al.: Strain and elasticity imaging in compression optical coherence elastography: the two-decade perspective and recent advances (2021). https://doi.org/10.1002/jbio.202000257